Title
Light-Driven Ultrafast Polarization Manipulation in a Relaxor Ferroelectric

Journal
Nano Letters, 22(23)

ISSN
1530-6984

Authors
Park, Suji
Wang, Bo
Yang, Tiannan
et al.

Publication Date
2022-12-14

DOI
10.1021/acs.nanolett.2c02706

NANO LETTERS

pubs.acs.org/NanoLett

Letter

Light-Driven Ultrafast Polarization Manipulation in a Relaxor Ferroelectric

Suji Park, Bo Wang, Tiannan Yang, Jieun Kim, Sahar Saremi, Wenbo Zhao, Burak Guzelturk, Aditya Sood, Clara Nyby, Marc Zajac, Xiaozhe Shen, Michael Kozina, Alexander H. Reid, Stephen Weathersby, Xijie Wang, Lane W. Martin, Long-Qing Chen, and Aaron M. Lindenberg*

Cite This: *Nano Lett.* 2022, 22, 9275−9282

Read Online

ACCESS | Metrics & More | Article Recommendations | Supporting Information

ABSTRACT: Relaxor ferroelectrics have been intensely studied for decades based on their unique electromechanical responses which arise from local structural heterogeneity involving polar nanoregions or domains. Here, we report first studies of the ultrafast dynamics and reconfigurability of the polarization in freestanding films of the prototypical relaxor $0.68PbMg_{1/3}Nb_{2/3}O_3$-$0.32PbTiO_3$ (PMN-0.32PT) by probing its atomic-scale response via femtosecond-resolution, electron-scattering approaches. By combining these structural measurements with dynamic phase-field simulations, we show that femtosecond light pulses drive a change in both the magnitude and direction of the polarization vector within polar nanodomains on few-picosecond time scales. This study defines new opportunities for dynamic reconfigurable control of the polarization in nanoscale relaxor ferroelectrics.

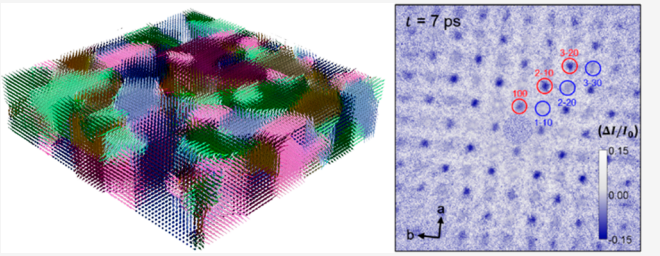

KEYWORDS: *ferroelectrics, structural dynamics, ultrafast, electron diffraction*

Relaxor ferroelectrics are a subgroup of ferroelectrics exhibiting characteristics such as dynamic polar nanoregions (PNRs) or polar nanodomains (PNDs), dynamic disorder and heterogeneity at the nanoscale, and unusually high dielectric and piezoelectric constants, enabling unique functionalities.[1−5] For example, $(1-x)PbMg_{1/3}Nb_{2/3}O_3$-$xPbTiO_3$ (PMN-xPT) and $(1-x)PbZn_{1/3}Nb_{2/3}O_3$-$xPbTiO_3$ (PZN-xPT) show ultrahigh electromechanical[6] and nonlinear[7] responses. The highest performance is attained for compositions near the morphotropic phase boundary (MPB),[8] where for PMN-0.32PT the crystal structure lies between a rhombohedral and tetragonal phase with the actual structure still being the subject of debate.[9,10] Recent studies reported the existence of intermediate monoclinic phases as it transforms from the rhombohedral to tetragonal phases, associated with a polarization rotation.[11−14] Additional studies have reported polarization rotation induced by temperature, electric fields, and stress,[15−17] thought to underlie the anomalous electromechanical response of the relaxors and other ferroelectrics and the mechanisms for polarization switching.[16,18,19] The intrinsic time scales for these processes to occur have not been measured, of central importance to the application of these materials within switchable devices. In particular, the intrinsic dynamic and nanoscale nature of the PNDs and associated low-energy barriers[9] indicate the potential for new opportunities for modulating the ferroelectric polarization on ultrafast time scales.[20−27]

Here, the light-induced ultrafast structural changes of an unpoled [001]-oriented PMN-0.32PT freestanding film are probed by fs MeV electron scattering. By measuring the structure factor of many Bragg peaks using an ultrafast crystallographic approach, we show that above-gap photoexcitation drives a reconfiguration of the polarization within PNDs on a few picosecond time scales. We propose a simple statistical model showing how the polarization distribution impacts the structure factor of a range of probed Bragg reflections. Our results indicate a significant light-induced reduction in the in-plane polarization within each PND, appearing in the ensemble-averaged diffraction measurement as a reduction in the in-plane mean square displacements. By combining these experimental results with phase-field simulations, we show that these atomic-scale changes can be understood in terms of an ultrafast modulation of the polarization magnitude coupled to a dynamic rotation of the polarization occurring on picosecond time scales. PMN-0.32PT 50 nm/$La_{0.7}Sr_{0.3}MnO_3$ (LSMO) 10 nm/$SrTiO_3$ (001) heterostructures were grown by pulsed-laser deposition

Received: July 9, 2022
Revised: November 11, 2022
Published: November 30, 2022

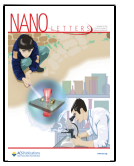

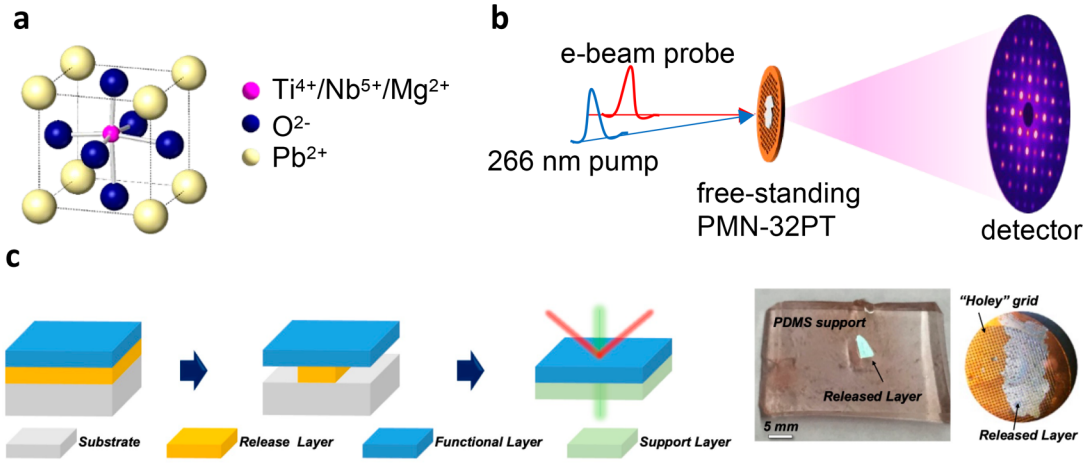

Figure 1. Structure of PMN-*x*PT and experimental setup: (a) Crystal structure of PMN-*x*PT; (b) 266 nm pump−UED probe experimental setup; (c) Freestanding relaxor membrane sample synthesis enabling transmission-mode experiment.

(see Figure 1 and the Supporting Information). Following growth, the PMN-0.32PT films were released from the substrate by selective etching of the sacrificial LSMO layer. The unclamped thin films were then removed from the substrate by slowly dipping the substrate in deionized water, leaving the freestanding films floating on the water surface. The released films were then moved to a secondary substrate (PDMS or "holey" grid) (Figure 1c).[28] We conducted femtosecond time-resolved electron diffraction measurements using the SLAC MeV-UED setup (Figure 1b).[29] Above-band-gap (4.5 eV) femtosecond optical pulses were used as a trigger on a PMN-0.32PT freestanding film ($E_g \approx 3.5$ eV),[30] probing the diffraction pattern using 3 MeV, 20 fC electron bunches at 180 Hz. By changing the delay time of the laser relative to the electron beam, we collected femtosecond-resolved diffraction patterns to capture the reversible structural response averaged over many shots and for a range of fluences from 2.6 to 7.8 mJ/cm^2.

Figure 2a shows the measured static electron diffraction pattern along the [001] zone axis at 28 K corresponding to (hk0) Bragg peaks where h, k, and l (=0) are the Miller indices of the reflection. From the images taken at each time delay, we extracted the intensity of the Bragg peaks, I_{hkl} and tracked the fractional intensity changes of each peak ($\Delta I/I_0$), where I_0 is the static intensity (corresponding to delay times $t < 0$). Figure 2b displays a representative image showing the differential intensity change at $t = 7$ ps. We note a strong anisotropy in the differential intensity changes for the measured Bragg reflections, with $h + k$ = odd peaks (red circles) showing a significant intensity drop as opposed to $h + k$ = even peaks (blue circles). The time-dependent intensity change of representative peaks with $h + k$ odd are shown in Figure 2c and $h + k$ even in Figure 2d. The graphs similarly show that the intensity of odd-parity peaks drops dramatically ($\frac{\Delta I}{I_0} \approx 10\%$) on few picosecond time scales (exponential fitted time constant ~2.1 ps) as opposed to even peaks showing much smaller changes. With increasing momentum transfer the effect becomes larger in both even and odd cases.

To understand the measured dynamic intensity changes of the Bragg peaks, we introduce a statistical structure factor model to capture how off-centering of the central B-site cations influence the scattered intensity of a given Bragg peak. We note that this model does not differentiate between whether the A- or B-site cations move—only their relative position determines the interference effects which define the intensity of each peak—and it ignores, to first order, any dynamic response from the oxygen octahedra. Although the nature of relaxors near the MPB is a mixture of various domains and crystal structures, i.e., rhombohedral (R), monoclinic (M), and tetragonal (T) phases,[11−13] here we assume a standard cubic perovskite structure as an averaged unit cell with an off-centered B-site

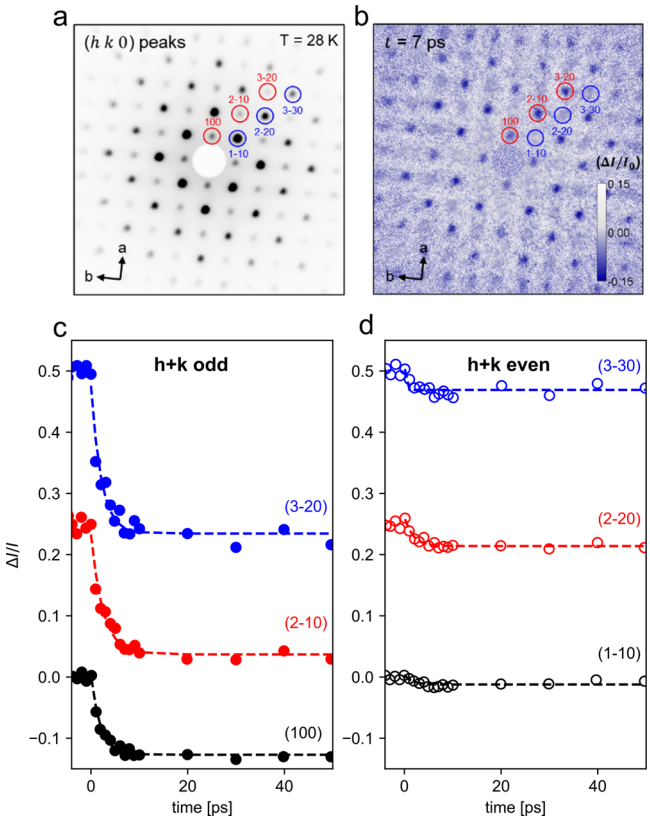

Figure 2. Transient diffraction pattern and time-resolved response of Bragg peaks. (a) Raw image showing UED diffraction data at 28 K probing along the [001] zone axis. (b) Fractional change $\Delta I/I = (I - I_0)/I_0$ at $t = 7$ ps. The red and blue circles define $h + k$ = odd and even peaks, respectively. (c, d) Intensity changes of representative odd (c) and even (d) peaks. Dashed lines are exponential fits with time constant ~2 ps.

https://doi.org/10.1021/acs.nanolett.2c02706
Nano Lett. 2022, 22, 9275−9282

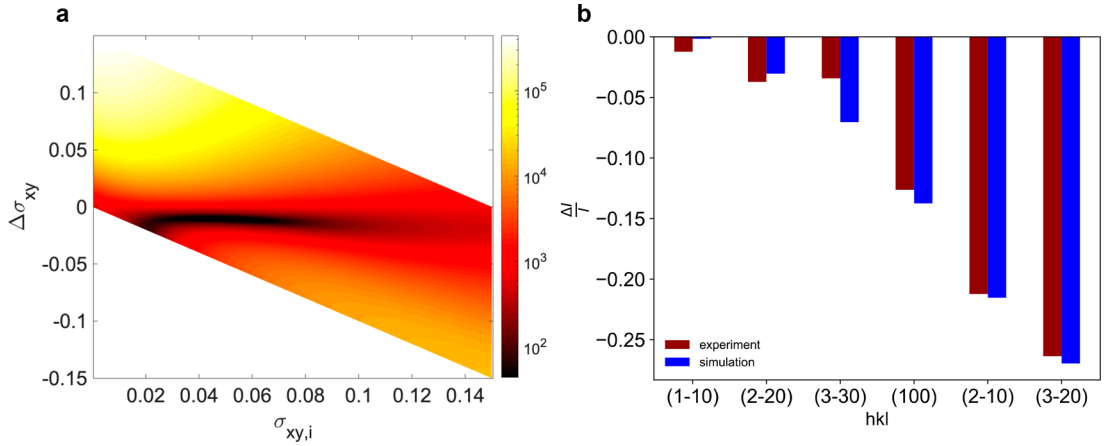

Figure 3. Structure factor model for change in unit cell. (a) Sum of squared residuals (SSR) as a function of the change in RMS displacements $\Delta\sigma_{xy}$ and the initial value $\sigma_{xy,i}$. Minimum SSR occurs at $\Delta\sigma_{xy} = -0.01$ at $\sigma_{xy,i} = 0.05$, indicating the RMS displacements of B-site atoms are reduced in the transient state. (b) Intensity changes at $t = 7$ ps comparing experiment to structure factor simulation.

cation displaced by small parameters δ_x, δ_y, and δ_z along the x, y, and z directions, respectively, with the z direction pointing along [001] (normal to the film). The intensity of the diffracted beam is determined from the structure factor, F_{hkl}, the Fourier transform of the unit cell, which can be written as

$$F_{hkl} = \sum_n f_n e^{2\pi i(hx_n + ky_n + lz_n)} \tag{1}$$

Here, f_n is the scattering factor of the nth atom. With a B-site cation at position $(1/2 + \delta_x, 1/2 + \delta_y, 1/2 + \delta_z)$ and for the [001] zone axis with $l = 0$, one obtains

$$F_{hk0} = \begin{Bmatrix} f_{Pb} - f_O - f_B e^{2\pi i(h\delta_x + k\delta_y)} & h + k \text{ odd} \\ f_{Pb} + 3f_O + f_B e^{2\pi i(h\delta_x + k\delta_y)} & h,\ k \text{ both even} \\ f_{Pb} - f_O + f_B e^{2\pi i(h\delta_x + k\delta_y)} & h,\ k \text{ both odd} \end{Bmatrix}$$

(2)where f_{Pb}, f_O, and f_B are the scattering factors for the lead, oxygen, and B-site atoms, respectively, and are assumed to be time independent. One may understand, from this expression, the origin of the bright and dark peaks shown in Figure 2A, with the weakest peaks associated with those with h+k odd where the scattering from the lead and B-site cations destructively interfere. To calculate the measured ensemble-averaged intensity, we note that the approximate diameter of a PND (~10 nm)[3] is larger than the transverse coherence of the electron beam (~1 nm). Thus, we compute the scattered intensity by first calculating the modulus squared of the unit cell structure factor $|F_{hkl}|^2$ and then ensemble averaging over all unit cells (corresponding to a no-interference condition of the scattered fields between different unit cells within a PND).[21,31] In the limit where the in-plane displacements δ_x and δ_y are small compared to the lattice spacing and isotropic, statistically averaging to zero such that there is no net polarization of the sample, we define the root-mean-square (RMS) displacements $\sqrt{\langle\delta_x^2\rangle} = \sqrt{\langle\delta_y^2\rangle} = \sigma_{xy}$ as a measure of the local unit cell dipole and assume negligible correlations between orthogonal displacements, e.g., $\langle\delta_x\delta_y\rangle = 0$. The measured intensity I_{hkl} can then be written as

$$I_{hk0} \propto \begin{Bmatrix} (A_{hk} - f_B)^2 + 4A_{hk}f_B\pi^2(h^2 + k^2)\sigma_{xy}^2 & h + k \text{ odd} \\ (A_{hk} + f_B)^2 - 4A_{hk}f_B\pi^2(h^2 + k^2)\sigma_{xy}^2 & h + k \text{ even} \end{Bmatrix}$$

(3)where A_{hk} includes the contributions from the lead and oxygen ions and is given by $A_{hk} = f_{Pb} + 3f_O$ if both h and k are even, otherwise $A_{hk} = f_{Pb} - f_O$. As noted above, this result is consistent with the observed static diffraction pattern dependence on the parity of $h + k$. It is also possible to understand from this result the origin of the anisotropy in the time-dependent response. Under the approximation that photoexcitation modulates the spread of in-plane RMS displacements by an amount $\Delta\sigma_{xy}$, we can write the normalized change in the intensity of the (hkl) peak as

$$\frac{\Delta I}{I} \approx \begin{Bmatrix} \dfrac{4A_{hk}f_B\pi^2(h^2 + k^2)\Delta\sigma_{xy}^2}{(A_{hk} - f_B)^2} & h + k \text{ odd} \\ \dfrac{4A_{hk}f_B\pi^2(h^2 + k^2)\Delta\sigma_{xy}^2}{(A_{hk} + f_B)^2} & h + k \text{ even} \end{Bmatrix}$$

(4)

In a model in which the light-induced modulation corresponds to a reduction in the RMS in-plane displacements corresponding to a reduction in the in-plane dipole within each PND, this equation predicts the observed strong dependence on the parity of $h + k$, with the largest effects for odd-parity reflections and with the intensity decreasing as experimentally observed for a decrease in the RMS spread of B-site cations. Significantly smaller amplitude changes are predicted by this model for the even reflections, as also observed experimentally: however, with opposite sign. One expects additional light-induced disorder in the form of Debye−Waller contributions[32] to all Bragg peaks associated with additional RMS disorder in the unit cell, which likely explains the smaller decreases observed for $h + k$ even.

In the following we apply a more detailed fitting procedure to check the validity of the above model and quantify the induced changes in the unit cell. We assume the distribution of B-site cations satisfies a Gaussian distribution, e.g., $\delta_n = N(\mu_n, \sigma_n^2)$ (for $n = x, y$) for both the static and

https://doi.org/10.1021/acs.nanolett.2c02706
Nano Lett. 2022, 22, 9275−9282

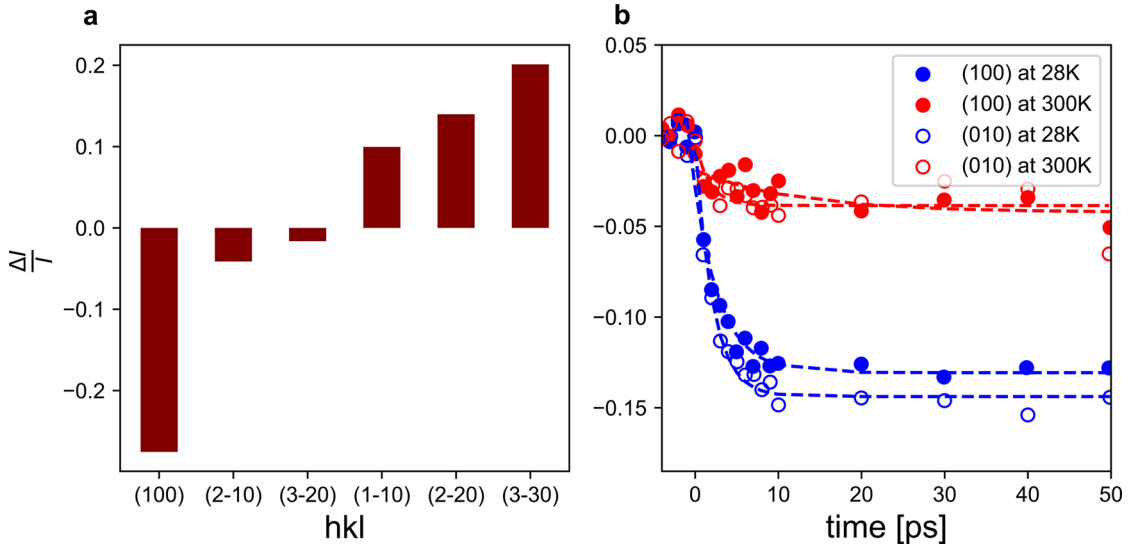

Figure 4. Temperature-dependent response. (a) Temperature-jump-induced fractional intensity changes of various peaks $\frac{\Delta I}{I} = \frac{I_{150\,K} - I_{28\,K}}{I_{28\,K}}$ (b) Transient response of PMN-PT comparing room temperature to 28 K for selected reflections.

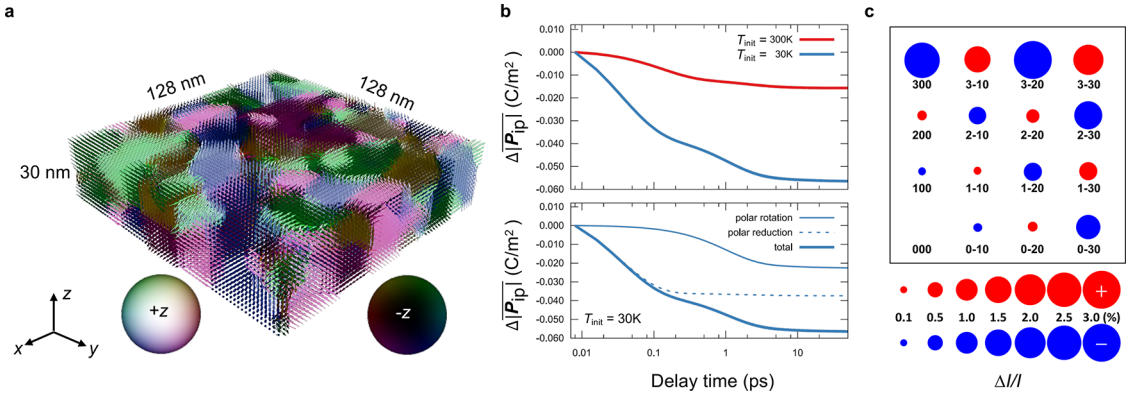

Figure 5. Phase-field simulations. (a) Phase-field simulation of the initial domain morphology and polarization configuration of the PMN-PT freestanding membrane. Simulated initial polarization spatial distribution in 3D for T_{init} = 30 K, showing the mosaic domain morphology and the characteristic domain size ∼10 nm. The 3D polarization vectors are colored by the direction of $\boldsymbol{P}_{ip} = (P_x, P_y)$ while the relative brightness corresponds to the magnitude and sign of P_z ($P_z > 0$, bright; $P_z < 0$, dark). (b) Phase-field simulation of the temporal evolution of the average change of in-plane polarization $\Delta|\overline{\boldsymbol{P}_{ip}}|$ (where $|\boldsymbol{P}_{ip}| = \sqrt{P_x^2 + P_y^2}$) after the onset of laser pulse at t = 0 ps. The upper panel shows $\Delta|\overline{\boldsymbol{P}_{ip}}|$ for two different initial temperatures, T_{init} = 30 K and T_{init} = 300 K. The lower panel shows the contribution to $\Delta|\overline{\boldsymbol{P}_{ip}}|$ due to polarization rotation (solid line), polarization reduction (dashed line), and their combination (curve with dots) for T_{init} = 30 K. The onset of the laser pulse is modeled as an instantaneous temperature jump with associated thermal expansion strains. (c) Calculated diffraction intensity changes $\Delta I/I$ for selected peaks around the origin in reciprocal space based on the polarization configurations obtained by phase-field simulations from t = 0 to t = 50 ps, for T_{init} = 30 K. The red (blue) color shows an increase (decrease) of the diffraction intensity while the radius denotes the amplitude of the change.

nonequilibrium structures.[33] First, we attempted to find the distribution of B-site cations in the *xy* plane before and after laser exposure. Using a least-squares method, we found the best fit where the combination of the initial and final distribution minimizes the sum of squared residuals, $\mathrm{SSR} = \sum\left(\frac{\Delta I_{exp}}{I_{exp,i}} - \frac{\Delta\langle I_{hkl}\rangle}{\langle I_{hkl}\rangle_i}\right)^2$. We calculated the SSR with all possible combinations of the initial and final distribution in the range of $0 < \sigma_{xy,i}$ (or $\sigma_{xy,f}$) < 0.15 with a step size of 0.0003. In order to capture the small amplitude and Q-dependent decreases in the even-parity peaks, we include for all reflections a standard Debye−Waller term as an additional means to modulate the intensity of each peak.[34] We present the SSR with respect to $\sigma_{xy,i}$ and $\Delta\sigma_{xy}$ in Figure 3a. The best fit was found at $\sigma_{xy,i}$ = 0.0492 and $\Delta\sigma_{xy}$ = −0.0105, corresponding to an approximately 20% reduction (∼5 pm) in the in-plane RMS displacements. The minimum SSR is achieved when $\Delta\sigma_{xy} < 0$ (Figure 3a) regardless of the initial distribution $\sigma_{xy,i}$. This result is consistent with the model presented above, indicating that the B-site cations moved toward the symmetrical position within the *xy* plane. Figure 3b shows that the intensity change of a range of six selected Bragg peaks calculated with the best-fit values $\sigma_{xy,i}$ and $\sigma_{xy,f}$ (blue bars) match well with the experimental data (maroon bars).

In order to understand the mechanism for the light-induced modulation of the unit cell, we also measured changes in the same PMN-0.32PT sample under a static temperature jump comparable to that estimated to be induced by the absorbed light pulse, approximately 100 K (see the Supporting

https://doi.org/10.1021/acs.nanolett.2c02706
Nano Lett. 2022, 22, 9275−9282

Information) and performed time-resolved measurements at various initial temperatures. Figure 4a shows the observed temperature-induced modulations comparing the Bragg peak intensities at 28 to 150 K. This shows effects qualitatively consistent with the structure-factor model presented above, with odd-parity reflections decreasing and even-parity reflections increasing. Therefore, this indicates the important role of a light-induced temperature jump in driving the observed reconfiguration of the structure toward a higher symmetry state. A similar decrease in the polar displacement and standard deviation of the Ti atom as a function of increasing temperature in PMN-25PT has recently been observed by neutron total scattering.[35] To further support the critical role of a temperature jump in the observed transient response, Figure 4b shows the transient response of the (100) reflection comparing room temperature (300 K) to the response at 28 K. This shows a dramatic increase in the magnitude of the distortions at low temperature and is consistent with the significantly smaller heat capacity of typical perovskite oxides at low temperature (c_p(30 K)/c_p(300 K) ≈ 1/7 for PZT[36]) leading to more significant photoinduced temperature changes at low temperature, assuming a constant absorbed pulse energy. A simple estimation using the known optical properties of PMN-xPT (Supporting Information) gives a temperature jump ΔT = 175 K for T_{init} = 30 K and ΔT = 25 K for T_{init} = 300 K. Finally we note also that the measured fluence-dependent response (Figure S5 in the Supporting Information) shows a roughly linear response up to the highest fluence measured (7.8 mJ/cm^2), consistent with this model. Additional electronic effects as have been observed in other studies[22,37−39] may be contributing separately to these responses, but one would expect depolarization-field screening effects, for example, to be less important within the disordered structure of the relaxors and for the freestanding films considered here.

To further evaluate the above model, we carried out phase-field simulations to characterize the dynamics of the polarization in response to a transient temperature jump, using this to establish a relation between the variation of polarization configurations and the change in diffraction-peak intensities which can be directly compared to the experimental results. The initial polarization configuration is obtained by evolving the system from a random-noise polarization distribution (Figure 5a). The resultant domain structure is characterized by a mosaic morphology consisting of nanosized domains with a characteristic length scale of ∼10 nm. The broadened peaks in the statistical distribution of in-plane polarization suggest the presence of a local monoclinic distortion of the lattice, resulting in the deviation of the polarization from the nominal $\langle 111\rangle_{pc}$ direction, as observed experimentally in relaxor crystals and freestanding membranes.[40,41] In the phase-field simulations transient photoexcitation is modeled as an instantaneous and spatially uniform temperature jump over the entire simulation system, accompanied by a uniform thermal strain due to thermal expansion (for a detailed description see the Supporting Information).

In response to the stimuli, the local ferroelectric polarization in the membrane will change in magnitude and direction to dissipate the injected energy. The variation of the averaged in-plane polarization $\Delta|\overline{\boldsymbol{P}_{ip}}|$ (where $|\boldsymbol{P}_{ip}| = \sqrt{P_x^2 + P_y^2}$ for each spatial point) with respect to the simulation time is plotted in Figure 5b, for two initial temperatures, T_{init} = 30 and 300 K, in order to compare to the experimental results. The simulation results show that $|\overline{\boldsymbol{P}_{ip}}|$ is reduced instantly upon the onset of the laser pulse and is saturated after ∼10 ps, consistent with the experimental results. A significantly enhanced reduction is seen for the case with low initial temperature, i.e., $\frac{\Delta|\overline{\boldsymbol{P}_{ip}}|\,(T_{init} = 30\ \mathrm{K})}{\Delta|\overline{\boldsymbol{P}_{ip}}|\,(T_{init} = 300\ \mathrm{K})} = 2.9$, which reasonably agrees with the intensity modulations in the experiment, i.e., $\frac{\Delta I / I(T_{init} = 30\ \mathrm{K})}{\Delta I / I(T_{init} = 300\mathrm{K})} \approx 3.3$. Figures S1−S4 in the Supporting Information show further calculations of the spatial distribution of the domains, the temperature dependence of the statistical distribution of the local polarization, and the relative contributions from a temperature jump compared to an associated elastic strain to the time-dependent polarization response. A closer examination of the temporal evolution reveals two features of polarization relaxation at different regimes before saturation: regime 1 from t = 0 to 0.1 ps and regime 2 from t = 0.1 to 10 ps. From the phase-field simulations, we find that the two regimes correspond to two mechanisms of polarization relaxation, namely, polarization reduction and polarization rotation, both of which contribute to the decrease of $|\overline{\boldsymbol{P}_{ip}}|$, as shown in the lower panel of Figure 5b. The polarization reduction occurs first in response to the laser pulse and dominates in regime 1 and saturates while the polarization rotation proceeds afterward in regime 2 and saturates at ∼10 ps reaching approximately 5° (Figure S3 in the Supporting Information). At the final saturated state (t = 50 ps), the polarization reduction corresponds to ∼60% of the overall change of $|\overline{\boldsymbol{P}_{ip}}|$ while the polarization rotation accounts for ∼40%.

To further corroborate the above model, we calculated the diffraction intensities of different Bragg peaks based on the phase-field simulations of the polarization response[42] (additional details are given in the Supporting Information). The percentage change of Bragg peak intensities upon applying the light pulse for T_{init} = 30 K is presented in Figure 5c. As seen, the simulated polarization response will cause an intensity decrease (blue circles) at peaks with indices $h + k$ odd and a significantly smaller increase (red circles) for $h + k$ even, consistent with experimental observations and the simple analytical model presented above. A list of the calculated Bragg peak intensities before and after light excitation is provided in Table S1 in the Supporting Information).

In summary, our time-resolved electron diffraction results show that the polarization state in the relaxor ferroelectric PMN-0.32PT can be significantly and reversibly modulated on picosecond time scales through above-gap photoexcitation. Using scattering approaches which provide access to the statistical properties of the relaxor polarization state and their dynamics, our measurements, combined with phase-field simulations, show that the polarization within polar nanodomains in relaxor ferroelectrics can be controlled in both magnitude and direction, in particular showing new possibilities for driving ultrafast polarization rotations. Experiments probing tilted samples would provide further information on the out-of-plane polarization dynamics. Additionally, exploration of other stochiometries near the morphotropic phase boundary would usefully inform the correlation between electromechanical responses and the dynamics of the polarization reported here. Finally, future efforts using nanofocused probe beams, diffuse scattering, and/

https://doi.org/10.1021/acs.nanolett.2c02706
Nano Lett. 2022, 22, 9275−9282

or the use of coherent imaging/speckle techniques in the time domain may enable direct probing of polarization dynamics and associated heterogeneous dynamics within electrically and optically biased operating devices[43] and new possibilities for controlling dynamic disorder and heterogeneity at the nanoscale.

■ ASSOCIATED CONTENT

Data Availability Statement

The data that support the findings of this study are available from the corresponding author upon reasonable request.

Supporting Information

The Supporting Information is available free of charge at https://pubs.acs.org/doi/10.1021/acs.nanolett.2c02706.

Sample synthesis, phase-field simulations, calculation of diffraction intensities from phase-field simulations, and fluence-dependent response (PDF)

■ AUTHOR INFORMATION

Corresponding Author

Aaron M. Lindenberg − *Stanford Institute for Materials and Energy Sciences, SLAC National Accelerator Laboratory, Menlo Park, California 94025, United States; Department of Materials Science and Engineering, Stanford University, Stanford, California 94305, United States; PULSE Institute, SLAC National Accelerator Laboratory, Menlo Park, California 94025, United States;* orcid.org/0000-0003-3233-7161; Email: aaronl@stanford.edu

Authors

Suji Park − *Stanford Institute for Materials and Energy Sciences, SLAC National Accelerator Laboratory, Menlo Park, California 94025, United States; SLAC National Accelerator Laboratory, Menlo Park, California 94025, United States;* Present Address: Center for Functional Nanomaterials, Brookhaven National Laboratory, Upton, NY 11973, USA

Bo Wang − *Department of Materials Science and Engineering, Penn State University, University Park, Pennsylvania 16802, United States*

Tiannan Yang − *Department of Materials Science and Engineering, Penn State University, University Park, Pennsylvania 16802, United States;* orcid.org/0000-0002-2071-4778

Jieun Kim − *Department of Materials Science and Engineering, UC Berkeley, Berkeley, California 94720, United States*

Sahar Saremi − *Department of Materials Science and Engineering, UC Berkeley, Berkeley, California 94720, United States; Materials Sciences Division, Lawrence Berkeley National Laboratory, Berkeley, California 94720, United States;* orcid.org/0000-0002-1625-8036

Wenbo Zhao − *Department of Materials Science and Engineering, UC Berkeley, Berkeley, California 94720, United States*

Burak Guzelturk − *Stanford Institute for Materials and Energy Sciences, SLAC National Accelerator Laboratory, Menlo Park, California 94025, United States;* Present Address: X-ray Science Division, Argonne National Laboratory, 9700 S. Cass Ave. Lemont, IL 60439, USA; orcid.org/0000-0003-1977-6485

Aditya Sood − *Stanford Institute for Materials and Energy Sciences, SLAC National Accelerator Laboratory, Menlo Park, California 94025, United States;* orcid.org/0000-0002-4319-666X

Clara Nyby − *Stanford Institute for Materials and Energy Sciences, SLAC National Accelerator Laboratory, Menlo Park, California 94025, United States*

Marc Zajac − *Stanford Institute for Materials and Energy Sciences, SLAC National Accelerator Laboratory, Menlo Park, California 94025, United States*

Xiaozhe Shen − *SLAC National Accelerator Laboratory, Menlo Park, California 94025, United States*

Michael Kozina − *SLAC National Accelerator Laboratory, Menlo Park, California 94025, United States*

Alexander H. Reid − *SLAC National Accelerator Laboratory, Menlo Park, California 94025, United States;* orcid.org/0000-0002-7587-295X

Stephen Weathersby − *SLAC National Accelerator Laboratory, Menlo Park, California 94025, United States*

Xijie Wang − *SLAC National Accelerator Laboratory, Menlo Park, California 94025, United States*

Lane W. Martin − *Department of Materials Science and Engineering, UC Berkeley, Berkeley, California 94720, United States; Materials Sciences Division, Lawrence Berkeley National Laboratory, Berkeley, California 94720, United States*

Long-Qing Chen − *Department of Materials Science and Engineering, Penn State University, University Park, Pennsylvania 16802, United States*

Complete contact information is available at: https://pubs.acs.org/10.1021/acs.nanolett.2c02706

Author Contributions

S.P., B.W., and T.Y. contributed equally.

Notes

The authors declare no competing financial interest.

■ ACKNOWLEDGMENTS

This work was primarily supported by the U.S. Department of Energy, Office of Science, Office of Basic Energy Sciences, under Award Number DE-SC-0012375. SLAC MeV-UED is supported in part by the DOE BES SUF Division Accelerator & Detector R&D program, the LCLS Facility, and SLAC under Contract Nos. DE-AC02−05-CH11231 and DE-AC02−76SF00515. B.G., A.S., C.N., and M.Z. acknowledge support by the Department of Energy, Office of Science, Office of Basic Energy Sciences, under contract DE-AC02-76SF00515. The work at UC Berkeley acknowledges the support of the Army Research Office under grant W911NF-21-1-0118, the National Science Foundation under grant DMR-2102895, and the Collaborative for Hierarchical Agile and Responsive Materials (CHARM) under cooperative agreement W911NF-19-2-0119. B.W. acknowledges support by the National Science Foundation (NSF) through Grant No. DMR-1744213. T.Y. and L.-Q.C. are supported as part of the Computational Materials Sciences Program funded by the U.S. Department of Energy, Office of Science, Basic Energy Sciences, under Award No. DE-SC0020145.

■ REFERENCES

(1) Cross, L. E. Relaxor ferroelectrics. *Ferroelectrics* **1987**, *76*, 241−267.

(2) Fernandez, A.; Acharya, M.; Lee, H.-G.; Schimpf, J.; Jiang, Y.; Lou, D.; Tian, Z.; Martin, L. W. Thin-film ferroelectrics. *Adv. Mater.* **2022**, *34*, 2108841.
(3) Li, F.; Zhang, S.; Damjanovic, D.; Chen, L.-Q.; Shrout, T. R. Ferroelectrics: Local Structural Heterogeneity and Electromechanical Responses of Ferroelectrics: Learning from Relaxor Ferroelectrics. *Adv. Funct. Mater.* **2018**, *28*, 1870262.
(4) Li, F.; Zhang, S.; Yang, T.; Xu, Z.; Zhang, N.; Liu, G.; Wang, J.; Wang, J.; Cheng, Z.; Ye, Z.-G.; Luo, J.; Shrout, T. R.; Chen, L.-Q. The origin of ultrahigh piezoelectricity in relaxor-ferroelectric solid solution crystals. *Nat. Commun.* **2016**, *7*, 13807.
(5) Takenaka, H.; Grinberg, I.; Liu, S.; Rappe, A. M. Slush-like polar structures in single-crystal relaxors. *Nature* **2017**, *546*, 391−395.
(6) Park, S.-E.; Shrout, T. R. Ultrahigh strain and piezoelectric behavior in relaxor based ferroelectric single crystals. *J. Appl. Phys.* **1997**, *82*, 1804−1811.
(7) Riemer, L. M.; Jin, L.; Uršič, H.; Otonicar, M.; Rojac, T.; Damjanovic, D. Dielectric and electro-mechanic nonlinearities in perovskite oxide ferroelectrics, relaxors, and relaxor ferroelectrics. *J. Appl. Phys.* **2021**, *129*, 054101.
(8) Krogstad, M. J.; Gehring, P. M.; Rosenkranz, S.; Osborn, R.; Ye, F.; Liu, Y.; Ruff, J. P. C.; Chen, W.; Wozniak, J. M.; Luo, H.; Chmaissem, O.; Ye, Z. G.; Phelan, D. The relation of local order to material properties in relaxor ferroelectrics. *Nat. Mater.* **2018**, *17*, 718−724.
(9) Manley, M.E.; Abernathy, D.L.; Sahul, R.; Parshall, D.E.; Lynn, J.W.; Christianson, A.D.; Stonaha, P.J.; Specht, E.D.; Budai, J.D. Giant electromechanical coupling of relaxor ferroelectrics controlled by polar nanoregion vibrations. *Science Advances* **2016**, *2*, No. e1501814.
(10) Eremenko, M.; Krayzman, V.; Bosak, A.; Playford, H. Y.; Chapman, K. W.; Woicik, J. C.; Ravel, B.; Levin, I. Local atomic order and hierarchical polar nanoregions in a classical relaxor ferroelectric. *Nat. Commun.* **2019**, *10*, 2728.
(11) Zhang, Y.; Xue, D.; Wu, H.; Ding, X.; Lookman, T.; Ren, X. Adaptive ferroelectric state at morphotropic phase boundary: Coexisting tetragonal and rhombohedral phases. *Acta Mater.* **2014**, *71*, 176−184.
(12) Singh, A. K.; Pandey, D. Evidence for M_B and M_C phases in the morphotropic phase boundary region of $(1-x)[Pb(Mg_{1/3}Nb_{2/3})O_3]-xPbTiO_3$: A Rietveld study. *Phys. Rev. B* **2003**, *67*, 064102.
(13) Wang, R.; Xu, H.; Yang, B.; Luo, Z.; Sun, E.; Zhao, J.; Zheng, L.; Dong, Y.; Zhou, H.; Ren, Y.; et al. Phase coexistence and domain configuration in $Pb(Mg_{1/3}Nb_{2/3})O_3$-0.34$PbTiO_3$ single crystal revealed by synchrotron-based X-ray diffractive three-dimensional reciprocal space mapping and piezoresponse force microscopy. *Appl. Phys. Lett.* **2016**, *108*, 152905.
(14) Kim, J.; Meyers, D. J.; Kumar, A.; Fernandez, A.; Velarde, G. A. P.; Tian, Z.; Kim, J.-W.; LeBeau, J. M.; Ryan, P. J.; Martin, L. W. Frequency-dependent suppression of field-induced polarization rotation in relaxor ferroelectric thin films. *Matter* **2021**, *4*, 2367−2377.
(15) Davis, M.; Damjanovic, D.; Setter, N. Electric-field-, temperature-, and stress-induced phase transitions in relaxor ferroelectric single crystals. *Phys. Rev. B* **2006**, *73*, 014115.
(16) Fu, H.; Cohen, R. E. Polarization rotation mechanism for ultrahigh electromechanical response in single-crystal piezoelectrics. *Nature* **2000**, *403*, 281−283.
(17) Li, F.; Zhang, S.; Yang, T.; Xu, Z.; Zhang, N.; Liu, G.; Wang, J.; Wang, J.; Cheng, Z.; Ye, Z.-G.; Luo, J.; Shrout, T. R.; Chen, L.-Q. The origin of ultrahigh piezoelectricity in relaxor-ferroelectric solid solution crystals. *Nat. Commun.* **2016**, *7*, 13807.
(18) Vasudevan, R. K.; Matsumoto, Y.; Cheng, X.; Imai, A.; Maruyama, S.; Xin, H. L.; Okatan, M. B.; Jesse, S.; Kalinin, S. V.; Nagarajan, V. Deterministic arbitrary switching of polarization in a ferroelectric thin film. *Nat. Commun.* **2014**, *5*, 4971.
(19) Prosandeev, S.; Xu, B.; Bellaiche, L. Polarization switching in the $PbMg_{1/3}Nb_{2/3}O_3$ relaxor ferroelectric: An atomistic effective Hamiltonian study. *Phys. Rev. B* **2018**, *98*, 024105.
(20) Mankowsky, R.; von Hoegen, A.; Först, M.; Cavalleri, A. Ultrafast Reversal of the Ferroelectric Polarization. *Phys. Rev. Lett.* **2017**, *118*, 197601.
(21) Chen, F.; Zhu, Y.; Liu, S.; Qi, Y.; Hwang, H. Y.; Brandt, N. C.; Lu, J.; Quirin, F.; Enquist, H.; Zalden, P.; Hu, T.; Goodfellow, J.; Sher, M. J.; Hoffmann, M. C.; Zhu, D.; Lemke, H.; Glownia, J.; Chollet, M.; Damodaran, A. R.; Park, J.; Cai, Z.; Jung, I. W.; Highland, M. J.; Walko, D. A.; Freeland, J. W.; Evans, P. G.; Vailionis, A.; Larsson, J.; Nelson, K. A.; Rappe, A. M.; Sokolowski-Tinten, K.; Martin, L. W.; Wen, H.; Lindenberg, A. M. Ultrafast terahertz-field-driven ionic response in ferroelectric $BaTiO_3$. *Phys. Rev. B* **2016**, *94*, 180104.
(22) Daranciang, D.; Highland, M. J.; Wen, H.; Young, S. M.; Brandt, N. C.; Hwang, H. Y.; Vattilana, M.; Nicoul, M.; Quirin, F.; Goodfellow, J.; Qi, T.; Grinberg, I.; Fritz, D. M.; Cammarata, M.; Zhu, D.; Lemke, H. T.; Walko, D. A.; Dufresne, E. M.; Li, Y.; Larsson, J.; Reis, D. A.; Sokolowski-Tinten, K.; Nelson, K. A.; Rappe, A. M.; Fuoss, P. H.; Stephenson, G. B.; Lindenberg, A. M. Ultrafast Photovoltaic Response in Ferroelectric Nanolayers. *Phys. Rev. Lett.* **2012**, *108*, 087601.
(23) Li, X.; Qiu, T.; Zhang, J.; Baldini, E.; Lu, J.; Rappe, A. M.; Nelson, K. A. Terahertz field−induced ferroelectricity in quantum paraelectric $SrTiO_3$. *Science* **2019**, *364*, 1079−1082.
(24) de la Torre, A.; Kennes, D. M.; Claassen, M.; Gerber, S.; McIver, J. W.; Sentef, M. A. Nonthermal pathways to ultrafast control in quantum materials. *Rev. Mod. Phys.* **2021**, *93*, 041002.
(25) Zhang, Y.; Dai, J.; Zhong, X.; Zhang, D.; Zhong, G.; Li, J. Probing Ultrafast Dynamics of Ferroelectrics by Time-Resolved Pump-Probe Spectroscopy. *Advanced Science* **2021**, *8*, 2102488.
(26) Prosandeev, S.; Grollier, J.; Talbayev, D.; Dkhil, B.; Bellaiche, L. Ultrafast neuromorphic dynamics using hidden phases in the prototype of relaxor ferroelectrics. *Phys. Rev. Lett.* **2021**, *126*, 027602.
(27) Disa, A. S.; Nova, T. F.; Cavalleri, A. Engineering crystal structures with light. *Nat. Phys.* **2021**, *17*, 1087−1092.
(28) Ji, D.; Cai, S.; Paudel, T. R.; Sun, H.; Zhang, C.; Han, L.; Wei, Y.; Zang, Y.; Gu, M.; Zhang, Y.; Gao, W.; Huyan, H.; Guo, W.; Wu, D.; Gu, Z.; Tsymbal, E. Y.; Wang, P.; Nie, Y.; Pan, X. Freestanding crystalline oxide perovskites down to the monolayer limit. *Nature* **2019**, *570*, 87−90.
(29) Weathersby, S. P.; Brown, G.; Centurion, M.; Chase, T. F.; Coffee, R.; Corbett, J.; Eichner, J. P.; Frisch, J. C.; Fry, A. R.; Gühr, M.; Hartmann, N.; Hast, C.; Hettel, R.; Jobe, R. K.; Jongewaard, E. N.; Lewandowski, J. R.; Li, R. K.; Lindenberg, A. M.; Makasyuk, I.; May, J. E.; McCormick, D.; Nguyen, M. N.; Reid, A. H.; Shen, X.; Sokolowski-Tinten, K.; Vecchione, T.; Vetter, S. L.; Wu, J.; Yang, J.; Dürr, H. A.; Wang, X. J. Mega-electron-volt ultrafast electron diffraction at SLAC National Accelerator Laboratory. *Rev. Sci. Instrum.* **2015**, *86*, 073702.
(30) Chan, K. Y.; Tsang, W. S.; Mak, C. L.; Wong, K. H.; Hui, P. M. Effects of composition of $PbTiO_3$ on optical properties of $(1-x)PbMg_{1/3}Nb_{2/3}O_3$-$xPbTiO_3$ thin films. *Phys. Rev. B* **2004**, *69*, 144111.
(31) Chen, F.; Zhu, Y.; Liu, S.; Qi, Y.; Hwang, H. Y.; Brandt, N. C.; Lu, J.; Quirin, F.; Enquist, H.; Zalden, P.; Hu, T.; Goodfellow, J.; Sher, M. J.; Hoffmann, M. C.; Zhu, D.; Lemke, H.; Glownia, J.; Chollet, M.; Damodaran, A. R.; Park, J.; Cai, Z.; Jung, I. W.; Highland, M. J.; Walko, D. A.; Freeland, J. W.; Evans, P. G.; Vailionis, A.; Larsson, J.; Nelson, K. A.; Rappe, A. M.; Sokolowski-Tinten, K.; Martin, L. W.; Wen, H.; Lindenberg, A. M. Reply to Comment on Ultrafast terahertz-field-driven ionic response in ferroelectric $BaTiO_3$. *Phys. Rev. B* **2018**, *97*, 226102.
(32) Lindenberg, A. M.; Johnson, S. L.; Reis, D. A. Visualization of atomic-scale motions in materials via femtosecond X-ray scattering techniques. *Annu. Rev. Mater. Res.* **2017**, *47*, 425−449.
(33) Blinc, R.; Dolinšek, J.; Gregorovič, A.; Zalar, B.; Filipič, C.; Kutnjak, Z.; Levstik, A.; Pirc, R. Local Polarization Distribution and Edwards-Anderson Order Parameter of Relaxor Ferroelectrics. *Phys. Rev. Lett.* **1999**, *83*, 424−427.

https://doi.org/10.1021/acs.nanolett.2c02706
Nano Lett. 2022, 22, 9275−9282

(34) Mannebach, E. M.; Li, R.; Duerloo, K.-A.; Nyby, C.; Zalden, P.; Vecchione, T.; Ernst, F.; Reid, A. H.; Chase, T.; Shen, X.; Weathersby, S.; Hast, C.; Hettel, R.; Coffee, R.; Hartmann, N.; Fry, A. R.; Yu, Y.; Cao, L.; Heinz, T. F.; Reed, E. J.; Dürr, H. A.; Wang, X.; Lindenberg, A. M. Dynamic Structural Response and Deformations of Monolayer MoS_2 Visualized by Femtosecond Electron Diffraction. *Nano Lett.* **2015**, *15*, 6889−6895.
(35) Liu, H.; Sun, Z.; Sun, S.; Zhang, Y.; Luo, H.; Qi, H.; Liu, L.; Neuefeind, J. C.; Xing, X.; Chen, J. Evolving Differentiated Local Polar Displacement and Relaxor Behavior in $Pb(Mg_{1/3}Nb_{2/3})O_3$−$PbTiO_3$ Perovskites. *Chem. Mater.* **2022**, *34*, 3985−3992.
(36) Lang, S. B.; Zhu, W. M.; Ye, Z. G. Specific heat of ferroelectric Pb(Zr1−xTix)O_3 ceramics across the morphotropic phase boundary. *J. Appl. Phys.* **2012**, *111*, 094102.
(37) Stoica, V. A.; Laanait, N.; Dai, C.; Hong, Z.; Yuan, Y.; Zhang, Z.; Lei, S.; McCarter, M. R.; Yadav, A.; Damodaran, A. R.; Das, S.; Stone, G. A.; Karapetrova, J.; Walko, D. A.; Zhang, X.; Martin, L. W.; Ramesh, R.; Chen, L. Q.; Wen, H.; Gopalan, V.; Freeland, J. W. *Nat. Mater.* **2019**, *18*, 377−383.
(38) Ahn, Y.; Everhardt, A. S.; Lee, H. J.; Park, J.; Pateras, A.; Damerio, S.; Zhou, T.; DiChiara, A. D.; Wen, H.; Noheda, B.; Evans, P. G. *Phys. Rev. Lett.* **2021**, *127*, 097402.
(39) Wen, H.; Chen, P.; Cosgriff, M. P.; Walko, D. A.; Lee, J. H.; Adamo, C.; Schaller, R. D.; Ihlefeld, J. F.; Dufresne, E. M.; Schlom, D. G.; Evans, P. G.; Freeland, J. W.; Li, Y. *Phys. Rev. Lett.* **2013**, *110*, 037601.
(40) Kumar, A.; Baker, J. N.; Bowes, P. C.; Cabral, M. J.; Zhang, S.; Dickey, E. C.; Irving, D. L.; LeBeau, J. M. Atomic-resolution electron microscopy of nanoscale local structure in lead-based relaxor ferroelectrics. *Nat. Mater.* **2021**, *20*, 62−67.
(41) Lindemann, S.; Irwin, J.; Kim, G.-Y.; Wang, B.; Eom, K.; Wang, J.; Hu, J.; Chen, L.-Q.; Choi, S.-Y.; Eom, C.-B.; Rzchowski, M.S. Low-voltage magnetoelectric coupling in membrane heterostructures. *Science Advances* **2021**, *7*, No. eabh2294.
(42) Yang, T.; Dai, C.; Stoica, V. A.; Xue, F.; Wang, H.; Ji, Y.; Gopalan, V.; Chen, L.-Q. Computing diffraction patterns of microstructures from phase-field simulations. *Acta Materialia* **2022**, *239*, 118258.
(43) Sood, A.; Shen, X.; Shi, Y.; Kumar, S.; Park, S.; Zajac, M.; Sun, Y.; Chen, L.-Q.; Ramanathan, S.; Wang, X.; Chueh, W. C.; Lindenberg, A. M. Universal phase dynamics in VO2 switches revealed by ultrafast operando diffraction. *Science* **2021**, *373*, 352−355.

https://doi.org/10.1021/acs.nanolett.2c02706
Nano Lett. 2022, 22, 9275−9282